

Magnetohydrodynamic effects of current profile control in reversed field pinches

C.R. Sovinec

Los Alamos National Laboratory,
Los Alamos, New Mexico

S.C. Prager

University of Wisconsin-Madison,
Madison, Wisconsin

United States of America

Abstract. Linear and non-linear MHD computations are used to investigate reversed field pinch configurations with magnetic fluctuations reduced through current profile control. Simulations with reduced ohmic drive and moderate auxiliary current drive, represented generically with an electron force term, applied locally in radius near the plasma edge show magnetic fluctuation energies that are orders of magnitude smaller than those in simulations without profile control. The core of the improved configurations has reduced magnetic shear and closed flux surfaces in some cases, and reversal is sustained through the auxiliary current drive. Modes resonant near the edge may become unstable with auxiliary drive, but their saturation levels can be controlled. The space of auxiliary drive parameters is explored, and the ill effects of deviating far from optimal conditions is demonstrated in non-linear simulations.

1. Introduction

The main impediment to better confinement in laboratory reversed field pinch RFP [1] experiments has been transport believed to be driven by the stochasticity of the magnetic field. Experimental studies [2–7] have provided strong evidence for the link between transport and magnetic field fluctuations, and computational studies [8–12] have provided substantial insight into the cause of the fluctuations. An ohmically driven pinch tends to a state with strong shear in the magnetic field and peaked plasma current. The toroidal magnetic field decreases monotonically with minor radius, passing through zero and reversing its direction in the plasma edge. Hence, the total magnetic field is toroidal on-axis and mostly poloidal at the edge. The applied electric field is toroidal, so the component of electric field that is parallel to the magnetic field is strong on-axis and weak at the plasma edge. The resulting current density profile has a gradient that, in a plasma with safety factor q below 1, drives resistive MHD instabilities. Saturation results from non-linear coupling to resonant stable fluctuations, leading to magnetic field stochasticity, and from quasi-linear modifications to the current density profile.

The spectrum of the saturated non-linear state is dominated by poloidal mode number $m = 1$ fluctua-

tions that are resonant at small radii and are driven linearly. They excite two non-linear cascades:

- (a) Coupling to robustly stable $m > 1$ fluctuations,
- (b) Coupling through $m = 0$ activity to $m = 1$ fluctuations that are resonant at large radii near the reversal surface (where $q = 0$) [10].

Quasi-linear feedback via the fluctuation induced electric field, $\mathbf{E}_f = -\langle \mathbf{v} \times \mathbf{b} \rangle$, where lower case indicates a perturbed quantity and $\langle \rangle$ is an average over the poloidal and toroidal directions, suppresses mean current near the magnetic axis and enhances mean current near the reversal surface [11]. The sustainment of poloidal current beyond paramagnetic effects, and hence of reversed toroidal field near the wall, constitutes the ‘MHD dynamo’. Recent numerical work shows that the non-linear activity becomes increasing intermittent and that the fluctuation level decreases weakly as the Lundquist number is increased [12]. The weak scaling compels us to look for means to enhance confinement over the ohmically driven RFP configuration.

The above description suggests that magnetic fluctuations and associated transport can be diminished by reducing the free energy source of the current density gradient. Applying auxiliary current drive at large radii and reducing the ohmic drive

can replicate and enhance the stabilizing effects of the quasi-linear feedback. Earlier MHD studies of current profile alteration with direct current helicity injection have demonstrated substantial reduction of magnetic fluctuations [13], and RF current drive has been suggested as an alternative means of auxiliary current drive [14–16]. Initial, rather coarse experimental attempts at current profile flattening by inductive means have proven extremely encouraging, decreasing the magnetic fluctuations by a factor of 2 and increasing energy confinement by a factor of 5 [17, 18].

In this article, we use linear eigenvalue computations and non-linear three dimensional simulations to examine the effects of current profile alteration on RFPs in the context of zero beta resistive MHD. This work reveals how different current density profile alterations either reduce or enhance the magnetic fluctuation level. The MHD equations typically used to describe RFP dynamics are augmented by auxiliary current drive terms which arise from an extra force in the electron equation of motion. We are not interested in treating the method of current drive, for example, RF or any other specific technique, but only the effect of current drive on MHD properties. Computation of energy transport changes with altered current profiles is beyond the scope of this article, but improved confinement can be expected for conditions demonstrating reduced magnetic fluctuation levels.

The linear calculations guide the useful placement of auxiliary current in non-linear simulations. The effects of the auxiliary current drive are incorporated into the equilibria studied linearly, where the important parameters are the auxiliary drive magnitude, radial location and width, and ohmic electric field. The stability of the set of modes which dominate typical RFP wavenumber spectra and non-linearly excite other fluctuations is used as a measure of success as the parameters are varied. We find ample regions where all the modes in the selected set are stable, indicating that high precision is not required from an auxiliary current drive system. The optimum profiles have a shallow parallel current gradient in the core resulting from a reduced inductive drive, and they have reversed field sustained by auxiliary drive applied near the plasma edge.

The non-linear simulations provide the saturated fluctuation amplitudes and indicate that profile control can reduce the energy in magnetic perturbations by 2 orders of magnitude or more. The amplitude of a particular mode is greatly reduced when it is predicted to be linearly stable and when modes resonant

at smaller radii are also stable. When all modes resonant within some radius are stabilized, they will have small but non-zero saturation amplitudes, since non-linear coupling with any remaining unstable modes keeps them from vanishing. In some cases, this allows the formation of closed flux surfaces in the plasma interior. In other cases where the magnetic field remains stochastic, confinement should still be substantially improved, since the effective thermal diffusivity is proportional to $\langle \bar{b}_r^2 \rangle$, the mean square of the radial component of the perturbed magnetic field [19–21]. For modes resonant near the plasma edge, the auxiliary drive can be destabilizing. In optimal conditions, these instabilities are weak, and the saturated amplitudes are smaller than those in typical RFP simulations due to the changes in non-linear couplings.

Current profile modification has been extensively investigated in tokamaks for achieving increased confinement and plasma beta. Improved performance has been demonstrated in tokamak experiments by using inductive effects [22–26], aided by neutral beam heating in some cases, and by using off-axis RF current drive [27, 28] to create high inductance and negative central shear profiles. While the intent of current profile control in RFPs is similar, confinement improvement is expected from reduced levels of global electromagnetic activity; not from suppressing localized electrostatic fluctuations as in tokamaks. In this respect, theoretical work on using current drive to stabilize linear tearing modes [29] and to suppress magnetic islands [30, 31] is more closely related to the topic considered here. However, the proximity of low order rational surfaces in RFPs precludes treating individual modes in isolation.

The remaining sections of this article are organized as follows: In Section 2 we describe the equations and numerical algorithms used in this study. The results of linear calculations are presented in Section 3, and the non-linear simulations are discussed in Section 4. Finally, Section 5 contains a discussion of our results and conclusions drawn from them.

2. Equations and numerical algorithms

The current gradient is the dominant source of free energy for sustaining magnetic fluctuations in present RFPs, so the pressureless limit of the MHD equations is relevant for exploring the effects of

current profile control. This set of equations includes a combined Ohm's–Faraday's equation and the centre of mass velocity equation. The important dimensionless parameters are the Lundquist number and the magnetic Prandtl number. These quantities are readily accessible when the equations are written in the dimensionless form,

$$\frac{\partial \mathbf{B}}{\partial t} = -\nabla \times \mathbf{E} = \nabla \times (S\mathbf{V} \times \mathbf{B} - \eta \mathbf{J} + \mathbf{E}_a) \quad (1)$$

$$\frac{\partial \mathbf{V}}{\partial t} = -S\mathbf{V} \cdot \nabla \mathbf{V} + S\mathbf{J} \times \mathbf{B} + \nu \nabla^2 \mathbf{V} + \mathbf{F}_a \quad (2)$$

where lengths are normalized by the minor radius a , magnetic induction by an approximate magnitude at $r = 0$, B_0 , time by the resistive diffusion time $\tau_r = 4\pi a^2/c^2\eta_0$ and velocity by the Alfvén speed, $v_a = B_0/(4\pi\rho)^{1/2}$. The mass density ρ is assumed to be fixed and uniform, and η in Eq. (1) is a dimensionless shape factor for electrical diffusivity. The important dimensionless parameters are then $S = \tau_r/\tau_a$ (Lundquist number, where $\tau_a = a/v_a$) and ν (magnetic Prandtl number). For the simulations discussed later, we note that the electric field is normalized by $e\eta_0 B_0/4\pi a$.

All computations use the straight, periodic cylinder approximation for the toroidal geometry of experiments. This is a common approximation for RFPs, since $q < 1$ across the entire radius, i.e. there are no regions of stabilizing magnetic curvature [32].

Equations (1) and (2) contain the source terms \mathbf{E}_a and \mathbf{F}_a , which represent auxiliary current drive. They may be considered body forces on the electrons (from RF current drive after averaging over the wave period, for example), in which case $\mathbf{E}_a = -\mathbf{F}_a/(\Omega_i\tau_a)$ relates the normalized fields, where Ω_i is the ion cyclotron frequency. The source is directed parallel to $\langle \mathbf{B} \rangle$, to control the $\lambda \equiv \langle \mathbf{J} \rangle \cdot \langle \mathbf{B} \rangle / \langle \mathbf{B} \rangle^2$ or 'parallel current' profile. The effect on the momentum density is small, and in some cases we have dropped the source term from (2) while retaining it in (1). The shape of these source terms is parameterized with three quantities, E_a , σ_a and r_a for a Gaussian distribution in radius,

$$E_a(r) = E_a \exp \left[-\left(\frac{r - r_a}{\sigma_a} \right)^2 \right]. \quad (3)$$

This distribution allows a systematic approach for varying the magnitude, location and width of the auxiliary current drive. It also approximates the current drive profile expected from ray tracing computations of lower hybrid waves [15, 16].

The following subsections describe numerical details for the linear and non-linear computations.

2.1. Linear calculations

To evaluate linear stability with respect to the current gradient, we employ asymptotic matching theory [33, 34] in pressureless conditions. Following standard procedure, we find eigenfunctions from the linear force-free condition, $\langle \mathbf{J} \rangle \times \mathbf{b} + \mathbf{j} \times \langle \mathbf{B} \rangle = 0$, with an ideal electric field in Faraday's law for the 'outer' regions. (Lower case indicates a perturbed quantity.) We also assume that $\langle \mathbf{V} \rangle \cong 0$. These conditions can be reduced to a scalar relation for the perturbed quantity $\psi \equiv r^{3/2}b_r/(m^2 + k^2r^2)^{1/2}$ associated with a single Fourier component [35],

$$\begin{aligned} \frac{d^2\psi}{dr^2} = \psi \left(\frac{m^2 + k^2r^2}{r^2} - \frac{m^4 + 10m^2k^2r^2 - 3k^4r^4}{4r^2(m^2 + k^2r^2)^2} \right) \\ - \lambda^2 + \frac{d\lambda}{dr} \left(\frac{m\langle B_z \rangle - kr\langle B_\theta \rangle}{m\langle B_\theta \rangle + kr\langle B_z \rangle} - \frac{2\lambda mk}{m^2 + k^2r^2} \right) \end{aligned} \quad (4)$$

where $\psi(r, \theta, z) \rightarrow \psi(r)e^{i(m\theta + kz)} + \text{c.c.}$, and c.c. denotes the complex conjugate of the previous term.

To determine the eigenfunction for a particular mode and a given equilibrium field, we numerically integrate Eq. (4) in the direction of increasing r across the distinct regions bounded by the axis, the wall and/or the resonance surfaces for the mode (where $q = -m/kR$, and R is the cylinder length divided by 2π). To find a sufficient number of linearly independent solutions, one integration is started from the left hand side of each region. At the axis, initial conditions for the integration are determined by regularity conditions, and at the resonance surfaces, it is convenient to start with a value of zero and unit slope. With the exception of the last region, integrations are extended across one resonance surface using Robinson's comparison equation [35]. This provides two linearly independent solutions (one new and one extended) in all but the first region.

When there is only one resonance surface for a mode, we label the solution starting from the axis ψ_0 and label the solution starting from the resonance surface ψ_i (Fig. 1). The general solution between the resonance surface and the wall, $\psi(r) = \psi_0(r) + C\psi_i(r)$, satisfies the 'constant ψ ' approximation [33] as $\psi_i = 0$ at the resonance surface ($r = r_s$). A particular solution satisfies the boundary condition at the wall when $C = -\psi_0(1)/\psi_i(1)$. The eigenvalue is then

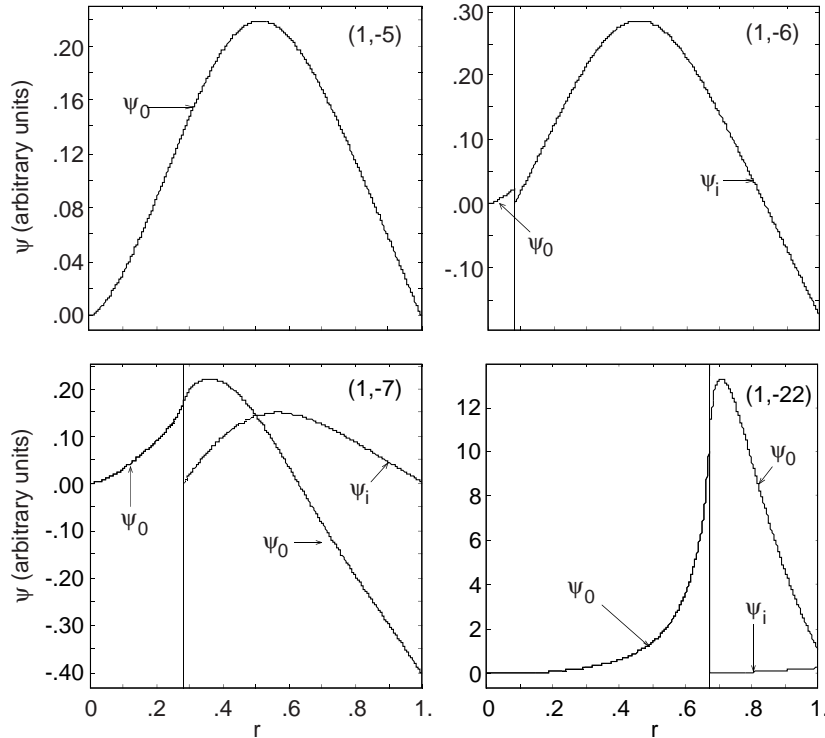


Figure 1. Solutions of Eq. (4) used to construct eigenfunctions for the paramagnetic equilibrium with $E_z = 3.95$ and $B_z(0) = 1$. The four plots show solutions for the (azimuthal, axial) Fourier components indicated, and the vertical lines mark the locations of the resonance surfaces. The (1,-5) mode does not have a resonance, and though close to marginal, $\psi_0(1) > 0$, so it is ideally stable. The (1,-6) mode is ideally unstable, since $\psi_i(1) < 0$. (In the second region, ψ_0 is not plotted for clarity.) For the (1,-7) mode, $\psi_i(1) > 0$ and $\psi_0(1) < 0$, so it is ideally stable (close to marginal) and resistively unstable. The (1,-22) mode is stable.

$$\Delta' \equiv \lim_{\varepsilon \rightarrow 0} \frac{\left. \frac{d\psi}{dr} \right|_{r_s+\varepsilon} - \left. \frac{d\psi}{dr} \right|_{r_s-\varepsilon}}{\psi|_{r_s}} = \frac{C}{\psi_0(r_s)} = -\frac{\psi_0(1)}{\psi_i(1)\psi_0(r_s)} \quad (5)$$

since ψ_0 does not contribute to the slope discontinuity at r_s ,¹ and ψ_i has unit slope just beyond r_s . The mode is unstable if $\Delta' > 0$, and a growth rate may be determined through a simple relation from the inner layer equations [33, 34]. Note that within the first region for each integration, the result is equivalent to Newcomb's ‘small’ solution [36, 37]. Thus, if it changes sign before crossing the first region, the

¹ The extended solution contains the logarithmic discontinuity, which is removed from the numerical integration by the comparison equation [35].

configuration is ideally unstable and resistive stability is not computed. Figures 1(a)–(d) show examples of solutions for two ideally unstable modes, one resistively unstable mode, and one mode that is both ideally and resistively stable.

In our parameter studies, we have also encountered modes with two resonance surfaces, but none with three or more, and the resistive stability determination is a little more complicated for these cases. Here we apply the double tearing theory of Dewar and Persson [38]. Our computed outer region solutions are used to construct the $\tilde{\psi}_{1-}$ and $\tilde{\psi}_{2-}$ functions discussed in Section VII of Ref. [38], and stability is determined without Doppler shifts.

We have verified that our linear calculations reproduce published marginal stability results for ideal and resistive modes in the paramagnetic equilibrium model [35] and in the ‘Bessel function model’ [39].

The paramagnetic equilibrium [40] is particularly important, since it represents what would result if MHD fluctuations had no effect on the electric field in the resistive MHD Ohm's law. The parallel current profile for zero beta conditions is

$$\lambda(r) = \frac{E_z \langle B_z(r) \rangle}{\eta(r) \langle B(r) \rangle^2}. \quad (6)$$

The uniform axial electric field sustains current along the magnetic field against the effects of resistive dissipation.

2.2. Non-linear simulations

To solve Eqs (1) and (2) including quasi-linear and non-linear effects, we have used the three dimensional simulation code, DEBS [41]. It applies the 'leapfrog' method, with velocity staggered in time from the vector potential, to advance the solution in discrete time steps from a given set of initial conditions. The dissipative terms in (1) and (2) are treated implicitly, while all non-linear advective terms employ a predictor-corrector method. In addition, a semi-implicit operator is used in Eq. (2) to avoid time step restrictions that would otherwise arise if the ideal MHD terms were handled explicitly [41]. The spatial representation is pseudo-spectral for the two periodic co-ordinates: differential operators are treated in the Fourier representation, while non-linear products are computed in configuration space. An efficient fast Fourier transform (FFT) routine is used to transform from one representation to the other. In the radial direction, a discrete representation is used, and radial derivatives are approximated by finite differences on a suitably staggered grid.

The normalized resistivity in Eq. (1) is considered a function of radius only. It has the form

$$\eta(r) = (1 + c_1 r^{c_2})^{c_3} \quad (7)$$

and the simulations discussed in Section 4 have the constants set to ($c_1 = 9$, $c_2 = 30$, $c_3 = 2$). This generates a profile that is uniform across most of the radial domain to isolate the MHD activity from resistivity gradient effects, as in Refs [8–13]. However, η rises sharply near the wall to approximate the suppression of current due to impurities and cold hydrogen. The isotropic viscosity in Eq. (2) is not intended as an accurate model for the anisotropic physical viscosity, but it is important for the numerical algorithm. We have used $\nu = 1$ in the simulations, and the resulting dissipation is typically small in comparison with the resistive dissipation associated with current density fluctuations.

For non-linear simulations, there are practical limitations on S and on the number of Fourier components that can be included. As S is increased, radial scale lengths decrease, requiring more computational mesh points. We have found that 125 mesh points provide good resolution for $S = 10^4$ simulations, and this level of refinement does not require an excessive amount of computer time. Although this value of S is about 2 orders of magnitude below present day RFP experiments, resistive tearing and the dominant non-linear couplings are not impeded by dissipation. The number of Fourier components included in a simulation also affects the computation time. We typically use $0 \leq m \leq 2$ and $-42 \leq n \leq 42$ ($n = kR$), which is sufficient resolution for cases with $R/a = 3$.

All non-linear simulations are started from an unstable paramagnetic equilibrium with small perturbations in the vector potential. There is a brief period of linear growth followed by quasi-linear and non-linear saturation. Non-linear interactions preclude a true steady state, but transients are small as modes exchange energy. (See Ref. [11] for a detailed description of the MHD activity in RFP simulations.) After saturation, we apply an increasing amount of auxiliary drive over a period of approximately $0.1\tau_r$ to gradually change the parallel current profile. The auxiliary drive is then held steady to give the fluctuations time to adjust to the new conditions. Reported results are averaged for at least $0.15\tau_r$ (many times the minor radius divided by the tearing growth rate) after the transients have settled out, since some degree of temporal fluctuation often remains.

3. Linear calculations

Here we ask what auxiliary current profiles stabilize the tearing modes resonant in the plasma core, with the expectation that any remaining fluctuations do not appreciably influence the magnetic configuration. The equilibria we examine satisfy the mean field Ohm's law, including the effect of the auxiliary current drive. The parallel current profile is described by

$$\lambda(r) = \frac{\langle E_z \rangle \langle B_z(r) \rangle}{\eta(r) \langle B(r) \rangle^2} + \frac{\langle E_a(r) \rangle}{\eta(r) \langle B(r) \rangle} \quad (8)$$

which is similar to Eq. (6); however, equilibria satisfying Eq. (8) may exhibit field reversal.² For a

² Since the auxiliary drive term represents an average of non-symmetric perturbations or effects not considered by MHD, Cowling's theorem [42] is not applicable.

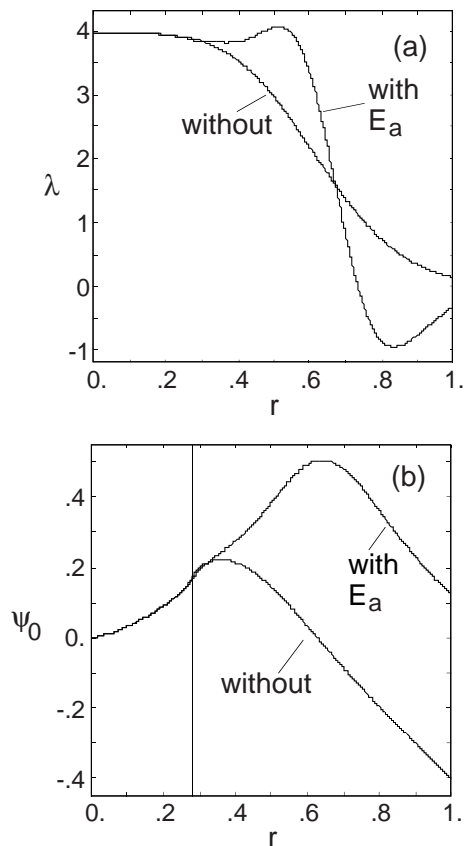


Figure 2. Comparisons of (a) parallel current profiles and (b) ψ_0 solutions for the (1,-7) mode of Fig. 1 with and without auxiliary current applied at $r = 0.6$. The resonance surface does not move in this case, and its location is shown as the vertical line in (b). The mode is stabilized by the auxiliary drive, since ψ_0 changes sign at the wall and ψ_i remains positive. Large distortions of the parallel current profile, such as the region of $\lambda < 0$ in this example, can be avoided; see Section 4.2.

given resistivity profile and axial flux Φ , the equilibrium is completely determined by the axial electric field and auxiliary current drive profile. The equilibria we study are realistic in that the corresponding auxiliary drive profiles are local in radius with the simple Gaussian shape of Eq. (3), consistent with expectations for an RF current drive system [15, 16], for example. Previous linear studies found equilibria stable to all current gradient driven modes [35, 43]. Though interesting, these equilibria may require global auxiliary drive to satisfy (8) with realistic resistivity profiles, which would be impractical for an experiment.

The localized auxiliary drive stabilizes a current gradient driven mode by flattening the λ profile in the region where the mode is sensitive to $d\lambda/dr$. For

resonant modes, the region of greatest sensitivity is near the resonant surface. As an example, consider the ψ solutions for the $m = 1, n = -7$ mode in Fig. 1, which indicates $\Delta' > 0$ according to Eq. (5). When auxiliary drive is applied at $r = 0.6$, the λ profile is flattened near the resonant surface, and the mode is stabilized (Fig. 2). The region where the λ gradient is negative still bends the solution towards 0. However, the bend is closer to the wall, and the denominator of the destabilizing term (the fourth term in Eq. (4)) is larger, so the mode is less sensitive to the displaced gradient.

An important result from the parameter study concerns the treatment of the axial electric field. With auxiliary drive at a fixed location, an adjustment of E_z can relocate a mode resonant surface to improve stability. If the resonant surface is at a radius which is too small to benefit from the auxiliary drive, decreasing E_z (with Φ fixed) increases the monotonically decreasing safety factor and moves the resonance outward. Conversely, an increase of E_z can improve stability for a mode resonant at too large a radius. We therefore consider a range of E_z in addition to a range of E_a for each auxiliary current position and width. With $r_a = 0.7$ and $\sigma_a = 0.15$, the stable regions for $m = 1, -8 \leq n \leq -5$ are displayed in Fig. 3. The $n = -5$ mode is not resonant in the upper left hand part of the investigated parameter space, but the other modes display a band of stability. Within a band, there is favourable alignment for the mode resonant surface and the auxiliary drive. Fortunately, the stable regions for individual modes overlap, so it is possible to find configurations where many are stable.

To assess the significance of r_a, σ_a and the resistivity profile, we determine the boundary of the stable region in E_a - E_z space for all modes in a set, while varying the auxiliary drive and resistivity shaping parameters. We choose to consider the set $m = 1, -9 \leq n \leq -3$, which includes the $m = 1$ modes that are normally resonant in the plasma core for $R/a = 3$. The stability diagram shown by Fig. 4 shows that as r_a is increased from 0.65 to 0.8, the stable region for the set drops to smaller values of E_z . Decreasing E_z maintains alignment between the flattened region of λ and the resonance surfaces of the modes in the set, as the auxiliary drive is moved outwards.

When the width of the auxiliary drive is increased, two effects are observed. First, the stable region is wider (Fig. 5). The auxiliary drive increases the parallel current over a larger fraction of the minor

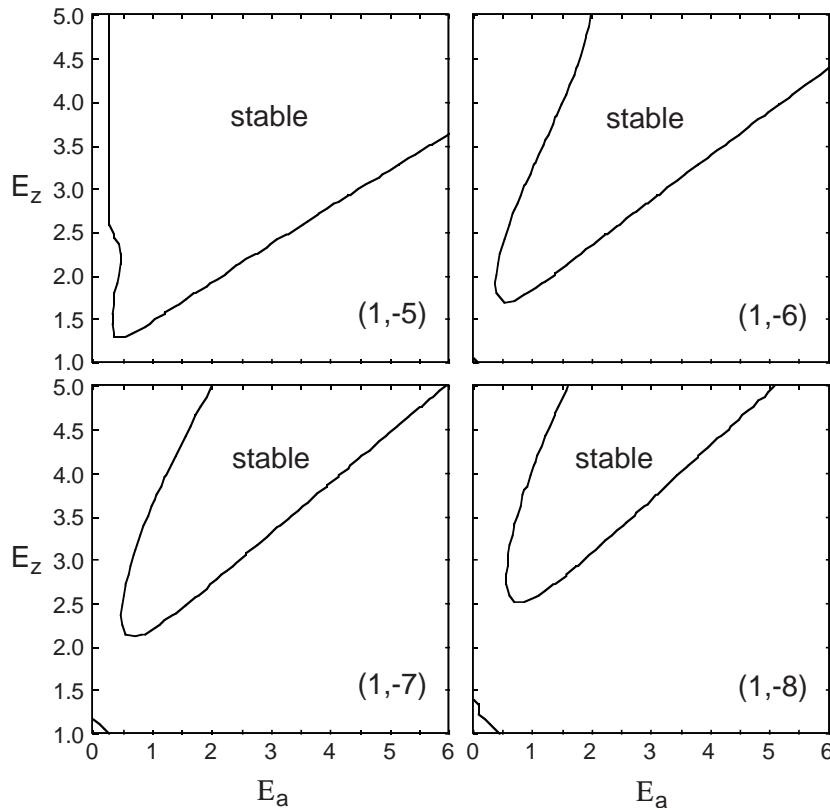


Figure 3. Regions of stability in the auxiliary drive/axial drive parameter space for the modes with the indicated (m, n) Fourier components. The auxiliary drive location and width are $r_a = 0.7$ and $\sigma_a = 0.15$, respectively, and the axial flux is $\Phi = 0.67$. The resistivity profile is $\eta(r) = (1 + 9r^{30})^2$. The axes are in the normalized electric field units of Eq. (1), where $E = 4\pi a E_{cgs} / c \eta_0 B_0$.

radius, so the matching of E_a and E_z values to provide stability is less sensitive. Second, the open end of the stable region is tilted to larger values of E_z as σ_a is increased. With the net axial flux held fixed, increasing σ_a increases parallel current and magnetic shear in the vicinity of r_a . For $r < r_a$, the safety factor increases, while for $r > r_a$, it decreases. Increasing E_z tends to offset the change in q within r_a , which maintains the alignment between r_a and the resonant surfaces. While a lack of extreme sensitivity is expected to be important in experiments, large amounts of inductive electric field are not desirable. This can be avoided by choosing parameters near the tip of the stable region.

We have also examined the influence of the resistivity profile. When the resistivity profile is broad (large values of c_2 in the resistivity shape function, Eq. (7)), the stable region lies at relatively small values of E_a as shown in Fig. 6. This is attributed to the

relatively small resistivity local to r_a , where inducing the same current density requires less driving force. The stable region also extends to smaller values of E_z . Less axial drive is needed to obtain the current, and hence shear, required to place all the resonance surfaces of modes in the set within r_a . Of greatest importance is that the stable region remains broad as the resistivity profile is changed, since this is likely to occur in an experiment when auxiliary current drive is added and energy confinement improves.

Computation of linear stability for modes outside the core resonant set have been carried out for equilibria that correspond to the specific conditions used in the non-linear simulations. In general, the equilibria with auxiliary drive tend to be unstable for $m = 0$ modes and for some $m = 1$ modes with $|n|$ values larger than those in the core resonant set. For these cases, the localized auxiliary drive sustains field reversal just outside r_a . This enhances $d\lambda/dr$ at the

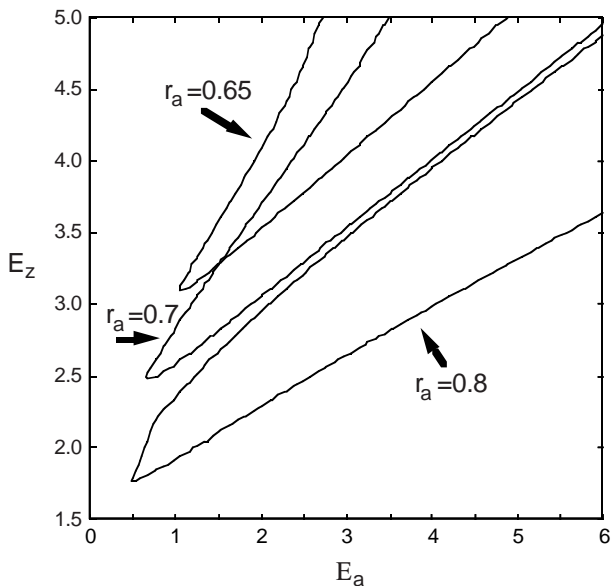


Figure 4. Regions of stability for the entire $m = 1$, $-9 \leq n \leq -3$ set with $\sigma_a = 0.15$ and r_a at the indicated values. For all curves $\Phi = 0.67$ and $\eta(r) = (1 + 9r^{30})^2$.

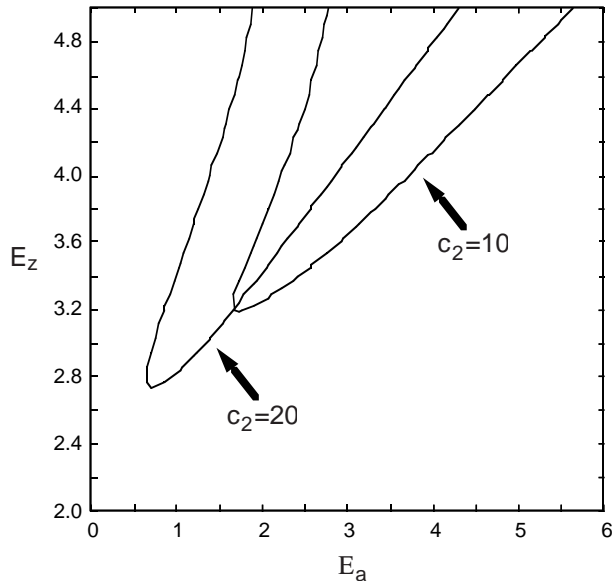


Figure 6. Regions of stability for the entire $m = 1$, $-9 \leq n \leq -3$ set with $r_a = 0.7$, $\sigma_a = 0.15$, and with the resistivity profiles varied such that c_2 has the indicated values, where $\eta(r) = 1 + 31r^{c_2}$. For both curves $\Phi = 0.67$.

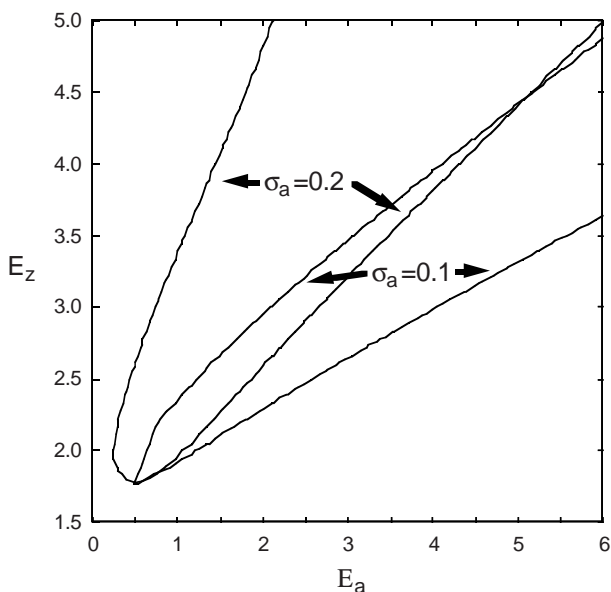


Figure 5. Regions of stability for the entire $m = 1$, $-9 \leq n \leq -3$ set with $r_a = 0.8$ and σ_a at the indicated values. For all curves $\Phi = 0.67$ and $\eta(r) = (1 + 9r^{30})^2$.

reversal surface for the mean axial field, where $q = 0$ and all $m = 0$ modes are resonant. The consequences of driving modes resonant outside r_a unstable are discussed in the next section.

4. Non-linear simulations

In this section we examine a series of non-linear simulations where auxiliary current drive is applied with various parameters. We compare the saturation amplitudes of the fluctuations with those of a typical case without auxiliary current drive. The zero beta conditions serve to isolate the current gradient driven MHD activity from the complications of pressure gradient driven activity and energy transport, in addition to simplifying the simulations. The merits of performing the linear calculations of the previous section are verified, as non-linear simulations with greatly reduced fluctuation levels are found in the region where the core resonant modes are stable. However, the auxiliary drive increases the saturation amplitude of the $m = 0$ modes in some cases, and this places further restrictions on the acceptable region of parameter space.

The investigation is divided into three parts. First, in Section 4.1, we compare two RFP simulations, one with and one without auxiliary drive, where the former is selected to demonstrate a significantly reduced magnetic fluctuation level. Second, in Section 4.2, we compare four simulations with the auxiliary drive applied at the same radius and with the same width, but with varied magnitudes and axial electric fields. This comparison demonstrates the ill effects of using

Table 1. Input parameters and resulting current and magnetic fluctuation levels for non-linear simulations

| Case | r_a | σ_a | E_a | E_z | Θ | F | RMS(b) ^a | $m = 0$ energy ^b | $m > 0$ energy ^b | Auxiliary power (%) |
|----------------|-------|------------|-------|-------|----------|--------|-------------------------|-----------------------------|-----------------------------|---------------------|
| A | — | — | 0 | 3.8 | 1.58 | -0.086 | 3.8×10^{-2} | 1.2×10^{-2} | 3.1×10^{-2} | — |
| B | 0.8 | 0.1 | 1.0 | 2.1 | 1.44 | -0.090 | 5.6×10^{-3} | 6.5×10^{-6} | 9.2×10^{-4} | 17 |
| C | 0.8 | 0.1 | 2.8 | 3.8 | 1.76 | -0.66 | 4.6×10^{-2} | 6.0×10^{-2} | 1.6×10^{-3} | 24 |
| D ^c | 0.8 | 0.1 | 2.8 | 3.0 | 1.64 | -0.60 | 4.1×10^{-2} | 5.0×10^{-2} | 3.2×10^{-6} | 31 |
| E | 0.8 | 0.1 | 2.8 | 2.1 | 1.51 | -0.52 | 3.3×10^{-2} | 3.2×10^{-2} | 7.8×10^{-4} | 43 |
| F | 0.65 | 0.1 | 2.8 | 3.8 | 1.90 | -0.52 | 2.4×10^{-2} | 1.4×10^{-2} | 2.9×10^{-3} | 25 |
| G | 0.65 | 0.1 | 1.5 | 3.4 | 1.71 | -0.16 | 2.0×10^{-2} | 4.0×10^{-3} | 7.4×10^{-3} | 17 |
| H | 0.8 | 0.2 | 1.2 | 3.0 | 1.67 | -0.40 | 1.2×10^{-2} | 4.4×10^{-3} | 5.5×10^{-8} | 21 |
| I | 0.8 | 0.2 | 0.75 | 2.1 | 1.46 | -0.12 | 5×10^{-7} | 4×10^{-15} | 8×10^{-12} | 19 |

^a The quantity RMS(b) is defined as $\sqrt{\frac{1}{R} \int_0^R dx |b|^2 / R}$, where b excludes the ($m = 0, n = 0$) Fourier component, and the bar indicates a temporal average.

^b The magnetic fluctuation energy associated with a group of poloidal modes is $\frac{1}{2} \sum_n \int dx \mathbf{b}_{m,n} \cdot \mathbf{b}_{m,n}^*$, where the summation is over $1 \leq n \leq 42$ for $m = 0$ and $-42 \leq n \leq 42$ for $m > 0$.

^c The $m > 0$ fluctuations for case D are small and decaying over the time when these results are averaged.

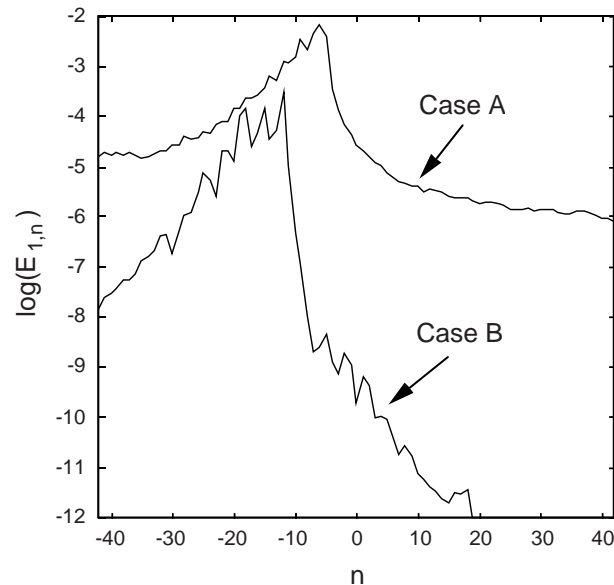


Figure 7. Comparison of magnetic energy spectra in the $m = 1$ Fourier components for cases A and B in Table 1. The magnetic energy in a Fourier component is $E_{m,n} = \frac{1}{2} \int dx \mathbf{b}_{m,n} \cdot \mathbf{b}_{m,n}^*$, and the results are averaged over $0.15\tau_r$.

parameters outside the stable region for the core resonant modes, and it indicates how to avoid an increase in the $m = 0$ activity. Third, in Section 4.3, the auxiliary drive radius and width parameters are discussed with respect to the linear and non-linear activity of modes outside the core resonant group examined in Section 3. These simulations show the benefits of large r_a and σ_a values.

4.1. Fluctuation reduction

An exemplary application of auxiliary drive is represented by case B in Table 1, which may be compared with the typical RFP simulation, case A. The auxiliary drive in B is applied at 80% of the wall radius with a width of 10%, plausible parameters for an RF current drive system [15]. The results show an 85% reduction in the RMS perturbed magnetic field or equivalently a 98% reduction in the magnetic fluctuation energy. These results are achieved through a moderate value of E_a in combination with a significantly reduced value of E_z . The configuration has nearly the same degree of reversal as case A, measured by the parameter $F \equiv \pi \langle B_z(r = 1) \rangle / \Phi$, and only 10% less axial current, indicated by the pinch parameter, $\Theta \equiv \pi \langle B_\theta(r = 1) \rangle / \Phi$. In the MHD power balance, 17% of the total input power comes from the auxiliary drive.

The auxiliary drive parameter set for case B is near the tip of the stable region for the core resonant modes plotted in Fig. 4 for $r_a = 0.8$. (The resistivity profile and axial flux used in the linear calculations match those of the non-linear simulations.) This makes the normally dominant modes linearly stable, and the non-linear fluctuation spectrum is dramatically altered. Figure 7 shows that the auxiliary drive has essentially eliminated all $m = 1$ Fourier components with $n > -10$. There remains a small amount of energy in these fluctuations due to non-linear coupling from unstable modes. In this case, the fluctuations are reduced enough to allow

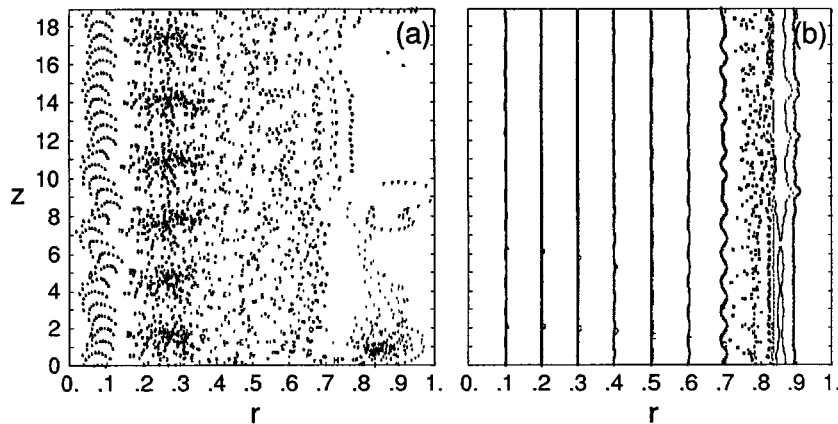


Figure 8. Poincaré surfaces of section for the $\theta = 0$ plane for (a) case A in Table 1 and (b) case B. The profile modification in case B leads to closed magnetic flux surfaces in the core, whereas the original RFP has a stochastic field everywhere. These Poincaré plots are generated from DEBS output with the TUBE code written by A.A. Mirin and D.A. Martin.

the formation of closed flux surfaces out to $r = 0.7$ (Fig. 8).

Comparing the location of the current gradient in the two cases, we observe that applying the auxiliary drive and reducing the axial field moves the gradient outward (Figs 9(a, b)). While this is stabilizing for $m = 1$ modes, it is destabilizing for $m = 0$ modes. The current profile from Eq. (8) with the same parameters as in case B is linearly unstable for the $m = 0, 1 \leq n \leq 61$ modes. In this case, the instability is weak, and the saturation amplitude of these modes in the non-linear simulation (with $\nu = 1$) is smaller than it is in case A. Without auxiliary drive, the $m = 0$ fluctuations are primarily sustained by non-linear coupling with the robustly unstable core resonant $m = 1$ modes [11]. Simulation B demonstrates that when auxiliary drive is successful, the reduced non-linear coupling into the $m = 0$ modes is more important for the saturation amplitudes than the linear destabilization.

Another observation from Fig. 9 is that the current profile from case B is nearly identical to that from Eq. (8) using the same parameters. The residual MHD activity is weak and therefore has little quasi-linear feedback on the $m = 0, n = 0$ fields. This contrasts with case A, where there is a large discrepancy between the paramagnetic equilibrium and the sustained RFP. In case B the auxiliary drive maintains the reversed field against resistive diffusion and effectively supplants the MHD dynamo.

In addition, a larger fraction of axial electric field drives mean current in the core, as opposed to driving fluctuations, so the axial current is nearly the same as that in case A despite the large reduction of E_z .

4.2. Varying the magnitudes of E_z and E_a

Among simulations with the same auxiliary drive radius and width but at different positions in the E_a - E_z parameter space, we observe significantly different saturated fluctuation amplitudes. Cases B to E in Table 1 have $r_a = 0.8$ and $\sigma_a = 0.1$. Cases C to E also have $E_a = 2.8$, but the different E_z values place D within the stable region for the core resonant modes in Fig. 4, with C above and E below. The resulting $m > 0$ energy in all three of these simulations is reduced from that of case A, and in case D it is essentially eliminated. In case C the $n = -7$ mode has the largest saturation amplitude of the $m = 1$ fluctuations, while the $n = -10$ mode is the largest in case E. Consistent with the discussion in Section 3, case C has E_z too large for all core resonant modes to benefit from the auxiliary drive at $r_a = 0.8$. In contrast, the larger $|n|$ modes in case E reside in the vicinity of a distortion in λ created by the auxiliary drive, which is relatively large for the small value of E_z .

The drawback of the parameters used in cases C to E is the resulting $m = 0$ activity, which is larger than that in case A. For a given amount of axial flux, $E_a = 2.8$ is excessive, and it creates a gross distortion

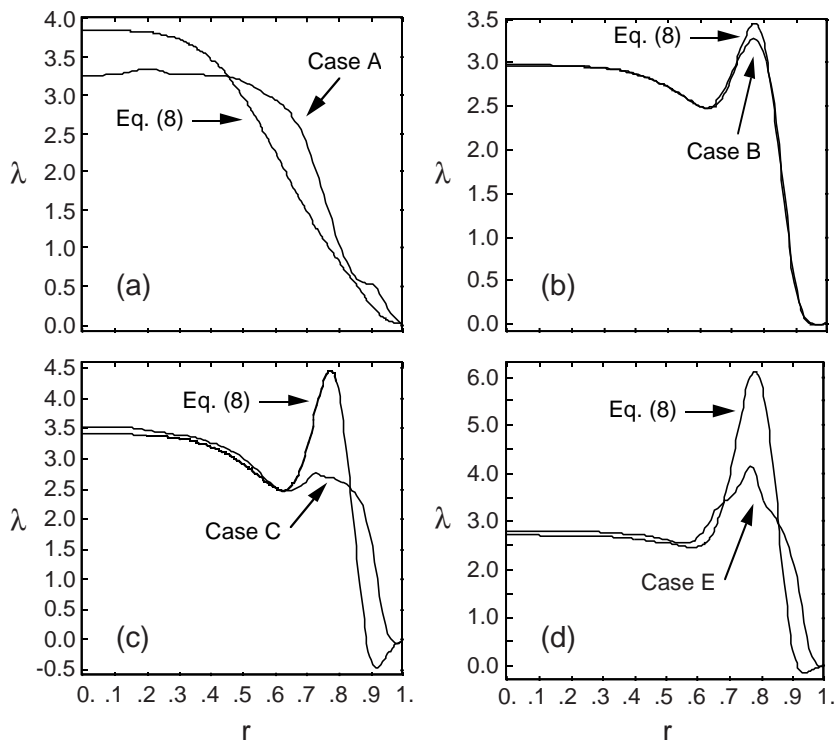


Figure 9. Comparison of the time averaged parallel current from the non-linear simulations indicated and the profiles represented by Eq. (8) with the same parameters. Discrepancies result from MHD activity, which is not considered in the derivation of profile (8).

of the λ profiles computed with Eq. (8). The gradients are destabilizing, and the resulting fluctuations in the non-linear simulations are effective at removing most of the distortion, see Figs 9(c, d). A significant fraction of the auxiliary power goes directly to the fluctuations instead of to the mean current, and since the $m = 0$ fluctuations are resonant near the distortion, they receive much of this power. In case B the distortion is much less pronounced (Fig. 9(b)), so the $m = 0$ fluctuations are not strongly excited.

The conditions most beneficial for reducing magnetic saturation amplitudes are those near the tip of the stable region of the linear calculations. These conditions apply a minimal amount of auxiliary drive, and hence a small current profile distortion near the reversal surface, while stabilizing the interior modes. That the reversal parameter in case B is similar to that in A is not a coincidence. The auxiliary drive and axial field are tuned to essentially replace the MHD dynamo without driving extra reversal.

4.3. Auxiliary drive radius and width parameters

When the auxiliary drive is applied at different radii, the fluctuation spectra reflect the proximity of the different mode resonant surfaces to r_a . Case F in Table 1 has the same values of E_a and E_z as case C, but $r_a = 0.65$. Referring again to Fig. 4, the parameters for F place it slightly below the stable region for the selected core resonant set. Its value of E_a creates too much parallel current at r_a , driving the large $|n|$ modes in the set unstable. The auxiliary drive is, nonetheless, sufficient to reduce the $m > 0$ energy in the non-linear simulation by more than an order of magnitude (like case C) from the standard RFP case. An undesirable feature of applying the auxiliary drive at small radii is the degree of $m = 1$ energy cascading to large $|n|$ through $m = 0$ components (Fig. 10(a)). Comparison with Fig. 7 indicates that this always happens to some extent; it is an important saturation mechanism in RFPs [10, 11]. However, the cascade is essentially driven by the

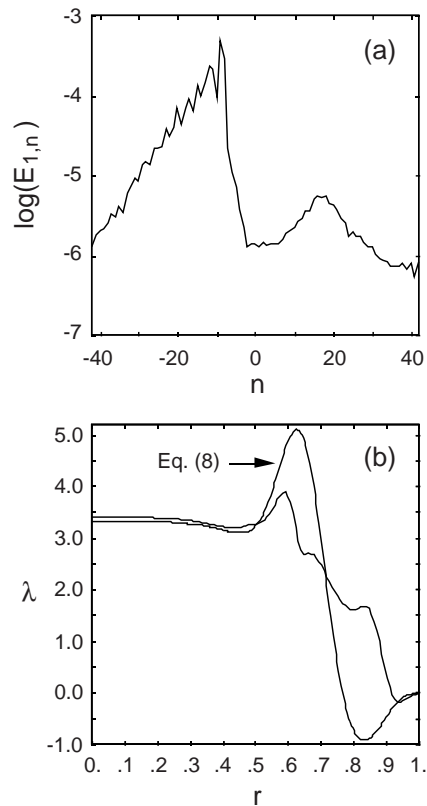


Figure 10. Results from simulation F in Table 1 with $r_a = 0.65$: (a) the time averaged $m = 1$ magnetic energy spectrum and (b) the time averaged parallel current profile, compared with the solution of Eq. (8) with similar parameters.

auxiliary current in case F, indicated by the discrepancy between the resulting parallel current and the solution to Eq. (8) shown in Fig. 10(b). The cascade starts from fluctuations resonant in the distortion, and since the conducting wall is further from the distortion, the excited fluctuations tend to be more unstable. This leaves a larger fraction of the radius, and a much larger fraction of the plasma volume, subject to stochastic magnetic field (Fig. 11).

The $m = 0$ fluctuation energy in case F is comparable to that in case A, less than in cases C–E. Having r_a inside the reversal surface makes the $m = 0$ modes less susceptible to destabilization. Reducing E_a and E_z to the parameters of case G in Table 1 places the configuration near the tip of the core resonant stable region in Fig. 4, and this reduces the $m = 0$ activity. However, the $m = 1$ mode cascading from $n = -10$ (beyond the range considered in the stability diagrams) is enhanced over that in case F. Since significant $m = 1$ activity seems unavoidable at

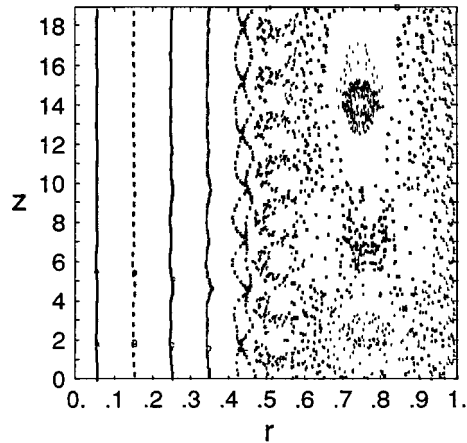


Figure 11. Poincaré surface of section for the $\theta = 0$ plane for case F in Table 1. The auxiliary drive is applied at a smaller radius than in case B, and a larger fraction of the plasma volume remains subject to stochastic magnetic field.

small r_a , applying the auxiliary drive at larger radii is preferable.

Increasing the auxiliary drive width allows smaller values of E_a for the same E_z , due to the tilt in the core resonant stable region shown in Fig. 5. This helps prevent an increase in the $m = 0$ activity when the auxiliary drive is applied. Case H has $r_a = 0.8$ and the same axial electric field as case D, but E_a is reduced to centre its position in the stable region for the larger auxiliary drive width, $\sigma_a = 0.2$, shown in Fig. 5. This produces very little $m > 0$ activity, and the $m = 0$ activity is less than that in case A. When E_a and E_z are reduced to the conditions near the tip of the stable region, as in case I, all magnetic fluctuations are essentially eliminated in the non-linear simulation.

The final observations concern the fraction of input power required of the auxiliary current drive system. The only simulations requiring less than 20% auxiliary drive (cases B, G and I) are those near the tips of the stable regions in Figs 4 and 5 for the respective values of r_a and σ_a . These configurations represent the smallest possible ohmic drive, in addition to the smallest possible auxiliary drive, for achieving stable core resonant modes. Since ohmic drive produces magnetic shear and a destabilizing current gradient in the core, it follows that cases with small ohmic drive are more easily improved. Furthermore, relaxing the auxiliary drive requirements leads to less distortion of the profile, hence less excitation of $m = 0$ modes and $m = 1$ modes resonant near the reversal surface, avoiding the situation where

auxiliary power drives fluctuations instead of mean current. Thus, configurations near the tips of the stable regions for the core resonant modes also have the lowest residual fluctuation levels.

5. Discussion and conclusions

The non-linear results of Section 4 demonstrate that auxiliary current drive with a realistic distribution can significantly improve the RFP configuration. The MHD dynamo is supplanted by the auxiliary drive, and the axial electric field is reduced to produce a current profile which has a core like that of a stable paramagnetic pinch. This suppresses the most destructive magnetic fluctuations, leading to an interior of closed flux surfaces under the best conditions. However, we have observed that the auxiliary drive must be applied with care. Excessive auxiliary power or current driven too far from the plasma edge sustains fluctuations over a large fraction of the plasma volume. Since auxiliary current drive (RF, DC helicity injection, etc.) is likely to have lower efficiency and greater complexity than ohmic power, it is fortunate that the smallest fluctuation levels result when the auxiliary power represents less than 20% of the total input power in the MHD simulations.

Sustaining some degree of magnetic field reversal is important to permit coupling between stable and unstable $m = 1$ modes through resonant $m = 0$ fluctuations [11]; it provides an important saturation mechanism and helps prevent disruptive excursions. Simulations with low fluctuation levels show that the reversal is sustained by the auxiliary drive. This diminishes the self-organizing aspect of MHD fluctuations in the final configuration, which is otherwise considered an inherent part of the RFP. However, self-organization can still play an important role. In practice, achieving a desired magnetic configuration quiescently through startup without encountering MHD activity will probably be difficult. The normal dynamo activity can keep the discharge close to the desired state as the auxiliary drive is applied and tuned.

The smallest fluctuation amplitudes in our study are produced with relatively broad auxiliary drive profiles centred near the plasma edge. Reproducing this in experiment may be difficult with a single current drive system, due to the large magnetic shear and plasma density gradient. Multiple systems may be able to produce a broad current drive profile, or even one of the completely stable configurations of previous linear studies [35, 43]. However, our results

show that a narrow profile, which is realistic for a single RF system [15, 16], can produce configurations with greatly reduced fluctuation levels.

In general, the results presented here, as well as previous experimental and computational results on current profile control, are very encouraging for RFP research. They suggest that the harmful transport associated with magnetic fluctuations may be suppressed. Determining what governs transport in a configuration with reduced current density driven fluctuations is an important topic for future research. The next computational step is to investigate the changes in energy confinement and the influence of pressure gradient driven modes by including a pressure evolution equation with anisotropic thermal conduction in the non-linear simulations. The effects of a temperature dependent resistivity profile may then be modelled, providing more detailed information regarding power requirements of the auxiliary drive system. A complete simulation will also include particle transport and a coupled auxiliary current drive calculation.

Acknowledgements

The authors wish to thank D. Schnack for his provision of and assistance with the DEBS code. This work is supported by the USDOE through Grant No. DE-FG02-85ER53212 and Contract No. W-7405-ENG-36.

References

- [1] Bodin, H.A.B., Newton, A.A., Nucl. Fusion **20** (1980) 1255.
- [2] Fiksel, G., Prager, S.C., Shen, W., Stoneking, M., Phys. Rev. Lett. **72** (1994) 1028.
- [3] Hattori, K., et al., Phys. Fluids B **3** (1991) 3111.
- [4] Ji, H., et al., Phys. Rev. Lett. **73** (1994) 668.
- [5] Nordlund, P., Mazur, S., Phys. Plasmas **1** (1994) 3936.
- [6] Chapman, B.E., et al., Phys. Plasmas **3** (1996) 709.
- [7] Ji, H., et al., Phys. Plasmas **3** (1996) 1935.
- [8] Schnack, D.D., Caramana, E.J., Nebel, R.A., Phys. Fluids **28** (1985) 321.
- [9] Kusano, K., Sato, T., Nucl. Fusion **30** (1990) 2075.
- [10] Holmes, J.A., et al., Phys. Fluids **31** (1988) 1166.
- [11] Ho, Y.L., Craddock, G.G., Phys. Fluids B **3** (1991) 721.
- [12] Cappello, S., Biskamp, D., Nucl. Fusion **36** (1996) 571.
- [13] Ho, Y.L., Nucl. Fusion **31** (1991) 341.

- [14] Shiina, S., et al., in 1992 International Conference on Plasma Physics (Proc. Conf. Innsbruck, 1992), Vol. 16C, Part II, European Physical Society, Geneva (1992) 917.
- [15] Uchimoto, E., et al., Phys. Plasmas **1** (1994) 3517.
- [16] Dziubek, R.A., Harvey, R.W., Hokin, S.A., Uchimoto, E., Nucl. Fusion **36** (1996) 453.
- [17] Sarff, J.S., Hokin, S.A., Ji, H., Prager, S.C., Sovinec, C.R., Phys. Rev. Lett. **72** (1994) 3670.
- [18] Stoneking, M.R., Lanier, N.E., Prager, S.C., Sarff, J.S., Sinitzyn, D., Phys. Plasmas **4** (1997) 1632.
- [19] Rechester, A.B., Rosenbluth, M.N., Phys. Rev. Lett. **40** (1978) 38.
- [20] Krommes, J.A., Oberman, C., Kleva, R.G., J. Plasma Phys. **30** (1983) 11.
- [21] Terry, P.W., et al., Phys. Plasmas **3** (1996) 1999.
- [22] Sabbagh, S.A., et al. Phys. Fluids B **3** (1991) 2277.
- [23] Ferron, J.R., et al., Phys. Fluids B **5** (1993) 2532.
- [24] Levinton, F.M., et al., Phys. Rev. Lett. **75** (1995) 4417.
- [25] Strait, E.J., et al., Phys. Rev. Lett. **75** (1995) 4425.
- [26] Fujita, T., et al., Phys. Rev. Lett. **78** (1997) 2377.
- [27] Hoang, G.T., et al., Nucl. Fusion **34** (1994) 75.
- [28] Litaudon, X., et al., Plasma Phys. Control. Fusion **38** (1996) 1603.
- [29] Westerhof, E., Nucl. Fusion **27** (1987) 1929.
- [30] Reiman, A.H., Phys. Fluids **26** (1983) 1338.
- [31] Lazzaro, E., Ramponi, G., Phys. Plasmas **3** (1996) 978.
- [32] Glasser, A.H., Greene, J.M., Johnson, J.L., Phys. Fluids **19** (1976) 567.
- [33] Furth, H.P., Killeen, J., Rosenbluth, M.N., Phys. Fluids **6** (1963) 459.
- [34] Coppi, B., Greene, J.M., Johnson, J.L., Nucl. Fusion **6** (1966) 101.
- [35] Robinson, D.C., Nucl. Fusion **18** (1978) 939.
- [36] Newcomb, W.A., Ann. Phys. (N.Y.) **10** (1960) 232.
- [37] Robinson, D.C., Plasma Phys. **13** (1971) 439.
- [38] Dewar, R.L., Persson, M., Phys. Fluids B **5** (1993) 4273.
- [39] Gibson, R.D., Whiteman, K.J., Plasma Phys. **10** (1968) 1107.
- [40] Bickerton, R.J., Proc. Phys. Soc. **72** (1958) 618.
- [41] Schnack, D.D., Barnes, D.C., Mikic, Z., Harned, D.S., Caramana, E.J., J. Comput. Phys. **70** (1987) 330.
- [42] Cowling, T.G., Q. J. Mech. Appl. Math. **10** (1957) 129.
- [43] Antoni, V., Merlin, D., Ortolani, S., Paccagnella, R., Nucl. Fusion **26** (1986) 1711.

(Manuscript received 5 August 1998
Final manuscript accepted 8 April 1999)

E-mail address of C.R. Sovinec:
sovinec@lanl.gov

Subject classification: C0, Rt; D2, Rt